Surface contact analysis in axial thrust bearings based on different numerical interpolation approaches

G Offner[1*], **M Lechner**[2], **K Mahmoud**[1], and **H H Priebsch**[3]
[1]Advanced Simulation Technologies, AVL List GmbH, Graz, Austria
[2]Industrial Mathematics Competence Center, Linz, Austria
[3]Acoustic Competence Center, Graz, Austria

The manuscript was received on 30 June 2006 and was accepted after revision for publication on 16 March 2007.

DOI: 10.1243/146441933JMBD85

Abstract: The simulation of moving parts in combustion engines and power trains by means of flexible multi-body dynamics requires complex computation techniques for the contact areas. Understanding surface interactions in detail is of great value for new products and can reduce the development time and costs significantly.

Modelling of lubricated contacts, which exist in slider bearings (axial and radial) and in the cylinder kit (piston, rings, and cylinder liner) are challenging tasks. Here, the simulation models have rough discretizations of the body surfaces and fine oil-film discretizations. Although body surfaces are usually given by finite element method (FEM) meshes, the non-linear reaction force of the loaded oil-film is determined by integrating the lubricant pressure field on the hydrodynamic mesh. The pressure is commonly calculated by solving a type of Reynolds equation in the gap between the contacting surfaces. The combination of different types of meshes of the body surfaces and the oil-film highly affects the quality of the results. Interpolation and integration approaches have to be capable of dealing with the high sensitivity of algorithms used for elastohydrodynamic contacts.

This paper presents an analysis of numerically simulated contacts in axial slider bearings for combustion engines. A surface contact algorithm with different numerical interpolation approaches for the clearance gap and its time derivative is utilized to investigate the elastohydrodynamic behaviour of axial thrust bearings. Thereby, the complete set of equations for moving and elastic bodies and oil-film reaction forces have to be solved in time domain to obtain the actual shape of the deformed clearance.

The numerical interpolation approaches comprise the Fritsch–Butland interpolation with the Brodlie-derivative-formulation as well as generalized cubic spline functions. The investigations consider effects of inclined crankshafts as they occur in axial thrust bearings of combustion engines. Detailed results are shown applying linear and tetragonal FEM meshes for the surfaces of the contacting bodies.

Keywords: flexible multi-body-dynamic system, elastohydrodynamic surface contact, numerical interpolation, finite-element method meshes, axial thrust bearing

1 INTRODUCTION

In the different stages of a modern engine development process, an increasing number of decisions are based on results derived from the simulation of virtual engines and power units under fired conditions. The requirements are to predict specific vibro-acoustic phenomena on one hand and to provide conclusions for optimum design solutions on the other with high precision and reliability.

These requirements lead to detailed models for all moving and vibrating parts of the engine. Although vibrating parts typically can be modelled with linear behaviour, contact areas of the moving parts behave

Corresponding author: Advanced Simulation Technologies, AVL List GmbH, Hans-List-Platz 1, Graz 8020, Austria. email: guenter.offner@avl.com

non-linear, in general. As the contact areas of the moving parts change with the engine rotation and the load distribution, very complex models have to be generated and a high amount of computational time is required for virtual results of high quality. Thus, another challenge is to deliver the results with maintainable effort of computational and handling time for a fully integrated simulation solution in the different stages of the development process.

The simulation of lubricated contacts, as they exist in engines at rotating parts (axial and radial slider bearings) and oscillating parts (piston and piston rings) has a long tradition. Nevertheless, reliable models for high prediction quality have been developed in the last 10 years, only. On one hand, a number of precise models for radial slider bearings have been published, already, because of their importance for the transfer of power in the engine. On the other hand, quite a few papers for axial slider bearings exist, although, the prediction of specific phenomena may be very important for engine noise and durability.

Furthermore, higher complexity is required for the hydrodynamic contact modelling in axial slider bearings. Because of the geometry of the rotating and contacting parts, structured models (beam, mass) as often used for models of radial slider bearings are not sufficient, anymore. The finite element method (FEM) meshes of the contacting surfaces are completely different and have to simulate inclination of shaft and block structure against one another as well as and deformation effects along the circumferential direction of the rotating bearing part. Thus the clearance geometry for the discretization of the oil film in between the contacting parts and the topology of the parts becomes more complex than for radial slider bearings. Accordingly, the integration and interpolation of pressure and deformation, respectively, have to be adapted for these requirements.

The paper presents a new approach to simulate axial slider bearings. On one hand, equations for moving and vibrating parts are separated from contact equations, to enable efficient numerical solutions in time domain. On the other hand, efficient algorithms for the numerical interpolation and integration in the contacts have to be applied, to simulate these contacts with maintainable effort.

2 MATHEMATICAL MODELLING OF BODIES

Because of the complexity of an elastic surface to surface contact of a flange and a thrust in an axial bearing, this mechanical system has to be broken down into coupled subsystems. Components, like the engine block and the crankshaft with linear elastic structural properties [**1**], have to be considered. The contacts of the components between each other e.g. in lubricated regions of an axial bearing contact have to be represented separately and will be investigated in section 3.

2.1 Equations of motion of a discrete body

The mathematical modelling of each body is based on Newton's equation of momentum and Euler's equation of angular momentum. This basis is well known in literature and can be found e.g. in reference [**2**]. With the fact given in reference [**3**], a 'floating frame of reference formulation' has been introduced for separating global (gross) motions and local vibration motions. This strategy introduces a moved reference coordinate system that moves in accordance with the gross motions of the elastic body. Elastic deformations are measured relative to this frame. The resulting ordinary differential equation (ODE) system [**4**], representing the dynamical properties of a body reads

$$\mathbf{M}\cdot\ddot{\boldsymbol{q}}+\mathbf{D}\cdot\dot{\boldsymbol{q}}+\mathbf{K}\cdot\boldsymbol{q}=\underbrace{\boldsymbol{f}^{\text{ext}}+\boldsymbol{f}^{\text{gyros}}-\boldsymbol{f}^{\text{rbAcc}}}_{f} \tag{1}$$

The matrices **M**, **D**, and **K** represent the structural properties of the body and are named mass, damping, and stiffness matrix. The vector of external forces and moments $\boldsymbol{f}^{\text{ext}}$ at the right-hand side of equation (1) is a sum of exciting joint forces and moments and external loads. External loads (e.g. gas force, valve train forces, and output torque) are given functions in time domain determined from given measurement or precalculated data. The highly non-linear terms of excitation loads are given by joints that connect one body to another (e.g. contact forces acting between a flange body and a thrust body of an axial bearing). The vector $\boldsymbol{f}^{\text{rbAcc}}$ contains the rigid body accelerations and reads

$$\boldsymbol{f}^{\text{rbAcc}}=\begin{pmatrix} m_1\cdot[\ddot{\boldsymbol{x}}_{\text{B}}+\mathbf{A}_{\dot{\Omega}}\cdot(\boldsymbol{x}_{\text{B}}+\boldsymbol{c}_1+\boldsymbol{u}_1)] \\ \boldsymbol{I}_1\cdot\dot{\boldsymbol{\Omega}} \\ \vdots \\ m_{\text{N}}\cdot[\ddot{\boldsymbol{x}}_{\text{B}}+\mathbf{A}_{\dot{\Omega}}\cdot(\boldsymbol{x}_{\text{B}}+\boldsymbol{c}_{\text{N}}+\boldsymbol{u}_{\text{N}})] \\ \boldsymbol{I}_{\text{N}}\cdot\dot{\boldsymbol{\Omega}} \end{pmatrix} \tag{2}$$

whereas the vector

$$\boldsymbol{f}^{\text{gyros}}=-\begin{pmatrix} m_1\cdot[2\cdot\mathbf{A}_{\Omega}\cdot(\dot{\boldsymbol{x}}_{\text{B}}+\dot{\boldsymbol{u}}_1) \\ +\mathbf{A}_{\Omega}^2\cdot(\boldsymbol{x}_{\text{B}}+\boldsymbol{c}_1+\boldsymbol{u}_1)] \\ -I_1\cdot\mathbf{A}_{\omega_1}\cdot\boldsymbol{\Omega}+(\mathbf{A}_{\Omega}+\mathbf{A}_{\omega_1}) \\ \cdot\boldsymbol{I}_1\cdot(\boldsymbol{\Omega}+\boldsymbol{\omega}_1) \\ \vdots \\ m_{\text{N}}\cdot[2\cdot\mathbf{A}_{\Omega}\cdot(\dot{\boldsymbol{x}}_{\text{B}}+\dot{\boldsymbol{u}}_{\text{N}}) \\ +\boldsymbol{A}_{\Omega}^2\cdot(\boldsymbol{x}_{\text{B}}+\boldsymbol{c}_{\text{N}}+\boldsymbol{u}_{\text{N}})] \\ -I_{\text{N}}\cdot\mathbf{A}_{\omega_{\text{N}}}\cdot\boldsymbol{\Omega}+(\mathbf{A}_{\Omega}+\mathbf{A}_{\omega_{\text{N}}}) \\ \cdot I_{\text{N}}\cdot(\boldsymbol{\Omega}+\boldsymbol{\omega}_{\text{N}}) \end{pmatrix} \tag{3}$$

represents the gyroscopic terms considered for the total elastic body.

From equation (1) both global (gross) motion quantities and local deformation can be calculated. A unique separation of these quantities needs to be made sure. For this purpose, additional conditions need to be stated that are discussed in reference [**4**]. According to this reference a projection strategy approach has been chosen for this purpose.

2.2 Reduction of the number of degrees of freedom

The total amount of computational time is significantly influenced by the number of degrees of freedom each body is represented with. Several methods can be applied to reduce the number of degrees of freedom significantly whereas the dynamical behaviour is sufficiently described. The reduced (condensed) number of degrees of freedom can be a subset of all degrees of freedom (static reduction), a set of linear combinations of all degrees of freedom (modal reduction) or a combination of both variants (mixed condensation). Details regarding these methods can be found in references [**5**] and [**6**]. According to these references, the reduced set of degrees of freedom $\boldsymbol{q}_a$ consists of physical degrees of freedom $\boldsymbol{q}_t$ of the uncondensed set as well as modal degrees of freedom z that represent the amplitudes of the linear combinations of the uncondensed system

$$\boldsymbol{q}_a = \begin{bmatrix} \boldsymbol{q}_t \\ z \end{bmatrix} \tag{4}$$

A transformation equation can be stated, that describes the relation between the physical degrees of freedom of the total system with the degrees of freedom of the calculation system, reading

$$\boldsymbol{q} = \mathbf{G}_{\mathrm{fa}} \cdot \boldsymbol{q}_a \tag{5}$$

Substituting the transformation equation (5) into equation (1) and multiplication with the transposed transformation matrix from left results in the equation of motion of the condensed system

$$\underbrace{(\mathbf{G}_{\mathrm{fa}}^t \cdot \mathbf{M} \cdot \mathbf{G}_{\mathrm{fa}})}_{\bar{\mathbf{M}}} \cdot \ddot{\boldsymbol{q}}_a + \underbrace{(\mathbf{G}_{\mathrm{fa}}^t \cdot \mathbf{D} \cdot \mathbf{G}_{\mathrm{fa}})}_{\bar{\mathbf{D}}} \cdot \dot{\boldsymbol{q}}_a + \underbrace{(\mathbf{G}_{\mathrm{fa}}^t \cdot \mathbf{K} \cdot \mathbf{G}_{\mathrm{fa}})}_{\bar{\mathbf{K}}} \cdot \boldsymbol{q}_a = \underbrace{\mathbf{G}_{\mathrm{fa}}^t \cdot \boldsymbol{f}}_{\bar{f}} \tag{6}$$

or

$$\bar{\mathbf{M}} \cdot \ddot{\boldsymbol{q}}_a + \bar{\mathbf{D}} \cdot \dot{\boldsymbol{q}}_a + \bar{\mathbf{K}} \cdot \boldsymbol{q}_a = \bar{\boldsymbol{f}} \tag{7}$$

$\bar{\mathbf{M}}$, $\mathbf{D}$, and $\bar{\mathbf{K}}$ denote the structural matrices of the condensed system. $\bar{\boldsymbol{f}}$ is the reduced vector of forces and moments. The reduced matrices together with the table of degrees of freedom and the geometry information are taken from finite-element (FE) software via an interface. Vibration analysis is performed on the reduced system only.

The transformation equation is also used for data recovery. Based on the solution of the reduced displacements $\boldsymbol{q}_a$, the displacement vector of the total body can be computed via the transformation equation (5).

3 MATHEMATICAL MODELLING OF LUBRICATED CONTACTS

3.1 Governing equations

The differential equation governing the generation of hydrodynamic pressure in an axial thrust bearing is derived from the conservation equation of mass and momentum. Using the approximations and assumptions commonly applied in the derivation of the Reynolds's equation yields

$$\frac{1}{r}\frac{\partial p}{\partial \phi} = \frac{\partial}{\partial y}\left(\eta \frac{\partial u}{\partial y}\right) \quad \text{and} \quad \frac{\partial p}{\partial r} = \frac{\partial}{\partial y}\left(\eta \frac{\partial w}{\partial y}\right) \tag{8}$$

Integrating equation (8) with respect to y and applying the boundary conditions

$$u(\phi, 0, z, t) = u_1, u(\phi, h, z, t) = u_2, w(\phi, 0, z, t) = 0, w(\phi, h, z, t) = 0 \tag{9}$$

results in

$$u = u_1 + (u_2 - u_1)\frac{Y}{h} + \frac{1}{r\eta}\frac{\partial p}{\partial \phi}\left(\frac{Y^2}{2} - \frac{hY}{2}\right) \quad \text{and}$$
$$w = \frac{1}{\eta}\left(\frac{\partial p}{\partial r} - \rho r \omega^2\right)\left(\frac{Y^2}{2} - \frac{hY}{2}\right) \tag{10}$$

A conformal mapping method is utilized to transform the end surface of the thrust bearing from its annular (physical) domain to a rectangular (computational) domain, taking into consideration the time dependency of the physical domain. A logarithmic function facilitates such domain transformation

$$\begin{aligned} x &= \phi \ \in \ 0 \leqslant x \leqslant 2\pi \\ \bar{y} &= y/\bar{h}(x, \bar{z}, t) \ \in \ 0 \leqslant \bar{y} \leqslant 1 \\ \bar{z} &= z_0(t) + \ln\left(\frac{r}{R_{\mathrm{in}}}\right) \ \in \ z_0(t) \leqslant \bar{z} \leqslant z_0(t) + \ln\left(\frac{R_{\mathrm{out}}}{R_{\mathrm{in}}}\right) \end{aligned} \tag{11}$$

where,

$$z_0(t) = \ln\left(\int_0^t u_2(\zeta)\, d\zeta / R_{\mathrm{in}}\right) \tag{12}$$

and

$$\bar{h} = f(c, e, \kappa, d) \tag{13}$$

The state variable $f(\phi, y, r, t)$ in the physical domain can be expressed in terms of the coordinate system in the computational domain by

$$f(\phi, y, r, t) = \bar{f}(x, \bar{y} \cdot \bar{h}, \bar{z}, t) \tag{14}$$

Substituting equation (11) in equation (10) yields

$$\bar{u}(x, \bar{y} \cdot \bar{h}, \bar{z}, t) = u_1 + (u_2 - u_1)\bar{Y} + \frac{\bar{h}^2}{\eta r}\frac{\partial \bar{p}}{\partial x}\left(\frac{\bar{Y}^2}{2} - \frac{\bar{Y}}{2}\right) \tag{15}$$

and

$$\bar{w}(x, \bar{y} \cdot \bar{h}, \bar{z}, t) = \frac{\bar{h}^2}{\eta}\left(\frac{1}{r}\frac{\partial \bar{p}}{\partial \bar{z}}\right)\left(\frac{\bar{Y}^2}{2} - \frac{\bar{Y}}{2}\right) \tag{16}$$

In order do be able to study the bearing performance even under cavitation, a fill ratio $\bar{\theta}$, $0 < \bar{\theta} < 1$, and effective density $\bar{\rho}_e = \bar{\theta} \cdot \bar{\rho}$ are introduce. In such case (for $\bar{\theta} = 1$ and $\bar{\rho}_e = \bar{\rho}$) a flooded region is defined as well as a cavitation region is given for $\bar{\theta} < 1$ and $\bar{\rho}_e = \bar{\theta} \cdot \bar{\rho}$.

Substituting the fill ratio and the effective density into the continuity equation and rearranging yields

$$\frac{\partial}{\partial x}\left(\frac{\overline{\rho\theta h^3}}{12\bar{\eta}}\frac{\partial \bar{p}}{\partial x} - \frac{1}{2}((u_1 + u_2)r - 2u_2 r^2)(\overline{\rho\theta h})\right) + \frac{\partial}{\partial \bar{z}}\left(\frac{\overline{\rho\theta h^3}}{12\bar{\eta}}\frac{\partial \bar{p}}{\partial \bar{z}}\right) = r^2\frac{\partial(\overline{\rho\theta h})}{\partial t} \tag{17}$$

3.2 Macro – hydrodynamics on rough surface (average Reynolds equation)

In order to consider rough contact surfaces, a high resolution in both spatial and time domain would be needed. Despite enhanced solver techniques, like e.g. multi-grid methods, an application in a dynamic simulation becomes inefficient. As a consequence the averaged method according to Patir and Cheng [**7**, **8**] is applied to solve the hydrodynamics problem on a macroscopic scale considering rough surfaces by stochastically evaluated flow factors or flow tensors. Using this technique, the average Reynolds equation for lubrication between two rough surfaces can be

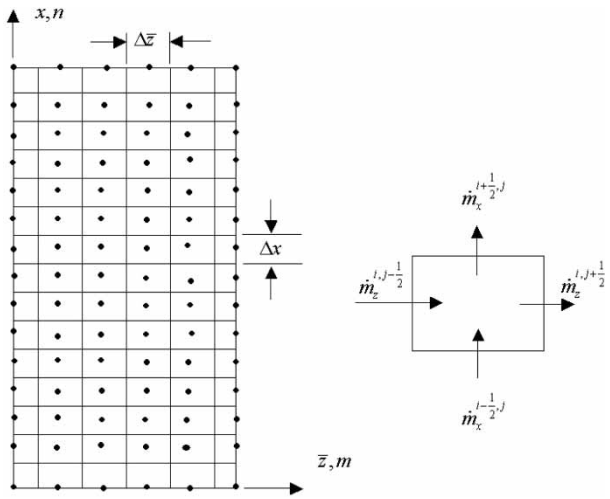

Fig. 1 Discretization stencil and control volume definition

written as follows

$$\frac{\partial}{\partial x}\left(\frac{1}{2}(\overline{\rho\theta}\sigma_c(u_1 - u_2)\Phi_s + ((u_1 + u_2)r - 2u_2 r^2)(\overline{\rho\theta h_T})) - \frac{\overline{\rho\theta h^3}}{12\bar{\eta}}\Phi_x\frac{\partial \bar{p}}{\partial x}\right) + \frac{\partial}{\partial \bar{z}}\left(-\frac{\overline{\rho\theta h^3}}{12\bar{\eta}}\Phi_{\bar{z}}\frac{\partial \bar{p}}{\partial \bar{z}}\right) = -r^2\frac{\partial(\overline{\rho\theta h_T})}{\partial t} \tag{18}$$

where

$$\sigma = \sqrt{\sigma_1^2 + \sigma_2^2} \tag{19}$$

and

$$\overline{h_T} = \bar{h} + \delta_1 + \delta_2 \tag{20}$$

As control volume approach is used to discritize equation (18), the domain of interest is unrolled and divided into n cells in x-direction and m cells in z-direction as shown in Fig. 1.

An enhanced method of 'successive over relaxation', [**9**, **10**] is applied to solve the discretized Reynolds equation (18). The method considers adaptive over or under relaxation and has the advantage of taking the results of the previous time step as start values when computing the results of the current time step.

4 SURFACE CONTACT ALGORITHM

The right-hand side of the equations of motion that were introduced in section 2.1 considers non-linear inertia terms as well as non-linear forces and moments that result from contacts to other bodies.

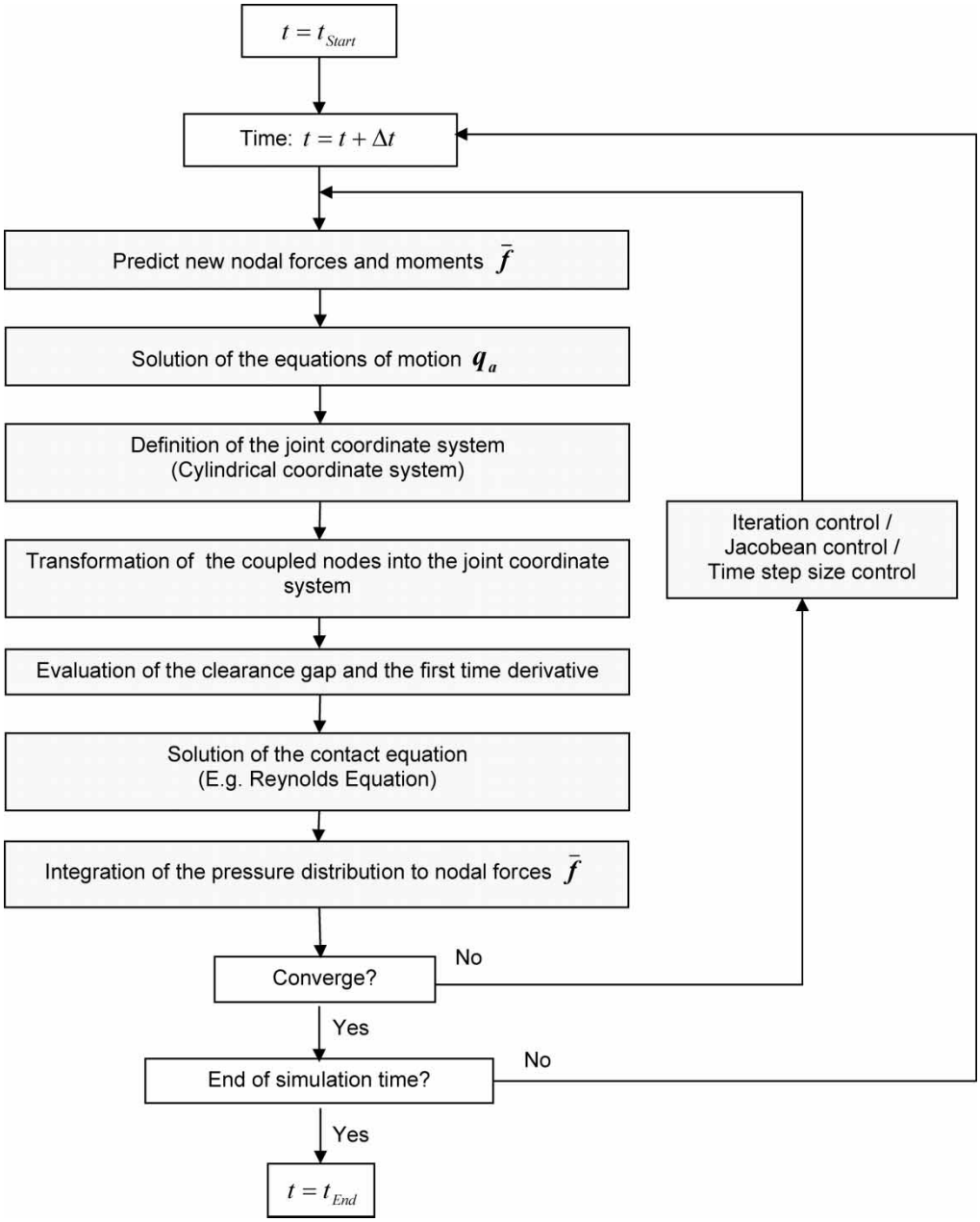

Fig. 2 Flow chart of a surface contact algorithm

Because of these non-linearities in addition to the large amount of degrees of freedom the integration in frequency domain cannot be done. Thus, an efficient integration in time domain needs to be performed. In order to minimize the numerical error, a direct implicit integration method (Newark's method) considering adjusted time step size is used for time integration. In each time step both the equilibrium in the equations of motion of the two bodies of the multi-body system and the equilibrium in the contact equations have to be satisfied. Figure 2 shows a flow chart of these steps.

The main focus of the contact algorithm is put on different numerical interpolation approaches for the evaluation of the clearance gap and its first derivation in time. In the result section it can be seen that the type of using interpolation approach affects the performance of the simulation process.

4.1 Solution of the equations of motion

The discrete condensed equations of motion of body 1 (21) and of body 2 (22) have to be solved in time domain by numerical time integration.

$$\bar{\mathbf{M}}_1 \cdot \ddot{\boldsymbol{q}}_{1,a} + \bar{\mathbf{D}}_1 \cdot \dot{\boldsymbol{q}}_{1,a} + \bar{\mathbf{K}}_1 \cdot \boldsymbol{q}_{1,a} = \bar{\boldsymbol{f}}_1 \tag{21}$$

$$\bar{\mathbf{M}}_2 \cdot \ddot{\boldsymbol{q}}_{2,a} + \bar{\mathbf{D}}_2 \cdot \dot{\boldsymbol{q}}_{2,a} + \bar{\mathbf{K}}_2 \cdot \boldsymbol{q}_{2,a} = \bar{\boldsymbol{f}}_2 \tag{22}$$

The solution of equations (21) and (22) considers predicted forces and moments for both bodies $\bar{f}_1$ and $\bar{f}_2$. From the solution of the condensed equations of motion, the shape of the clearance gap and its first time derivative are interpolated. Based on the interpolated functions $\bar{h}$ and $\partial\bar{h}/\partial t$ the contact pressure is evaluated and integrated to new nodal forces. A fixed point iteration scheme predicts new forces and moments based on the integrated nodal forces. If the convergence is not reached after a predefined number of iterations, the current time step size has to be reduced (if this is possible) or new Jacobean matrices for the surface contact evaluation need to be computed. A comprehensive description concerning the different numerical time integration methods can be found in references [**11**, **12**], and [**13**].

4.2 Definition of the joint coordinate system and the coordinate transformation

A new coordinate system for the contact evaluation, which is called joint coordinate system, has to be defined. The interpolation of the clearance gap and its first derivative in time, the solution of the hydrodynamics as well as the integration of the pressure distribution has to be done in this coordinate system. For the definition of this cylindrical coordinate system the origin and the orientation needs to be computed from the positions of the coupled nodes.

After the definition of the joint coordinate system, all positions and velocities of the connected nodes of both bodies have to be transformed from the Cartesian body coordinate systems into the cylindrical joint coordinate system.

4.3 Determination of the clearance gap and its first derivative in time

In order to solve the lubricated contact equation of a surface contact, the clearance gap and its first derivative in time have to be evaluated from the discrete node positions and velocities of the contacting body surfaces by numerical interpolation. For this purpose, a two-dimensional numerical interpolation has to be performed in the previous defined cylindrical joint coordinate system (section 4.2). For an axial thrust bearing, a numerical interpolation of the axial positions over the radial and circumferential coordinates has to be evaluated. During a simulation process the numerical interpolation has to be executed many times. Thus, the use of a highly efficient interpolation algorithm must be utilized.

With respect to the FE-discretization of the contacting surfaces, two different interpolation strategies can be distinguished.

If a regular FE-topology (only regular linear FE-elements) is used (Fig. 3 – left side), a special interpolation strategy can be applied. As the figure shows, a regular and rectangular distribution of the data points is given, for the FE-nodes and for the HD-nodes. Thus, the two-dimensional interpolation can be performed by applying a one-dimensional interpolation approach twice. For the one-dimensional interpolation two different approaches are discussed. On the one hand a high efficient method (Fritsch–Butland-interpolation) and on the other hand an accurate approach (generalized cubic spline interpolation) is utilized.

For irregular distributed data points (Fig. 3 – right side) a multiple application of a one-dimensional interpolation cannot be applied. In this case an efficient two-dimensional interpolation approach needs to be used, such as the modified Shepard

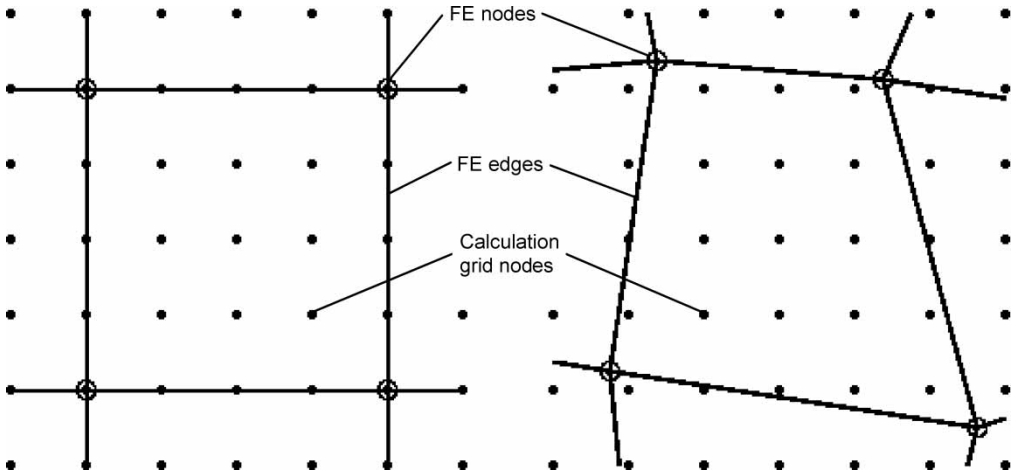

Fig. 3 Regular versus general FE – discretization

interpolation by Renka [**14**, **15**]. Compared with the multiple one-dimensional approach, these methods are more expensive in terms of CPU time. Considering the complex iteration and time integration scheme that is applied during one simulation run (Fig. 2), the simulation time is dominated by the interpolation of the FE-nodes and by the integration of the computed pressure to nodal forces. As a consequence, the whole dynamic simulation of these models becomes inefficient. Furthermore, the need of regular FE topologies of the contacting surfaces can easily be considered, when modelling the contacting surfaces in the preprocessing step. Thus, the usage of general FE-topologies is not discussed in this paper.

4.3.1 *Fritsch–Butland-interpolation*

The Fritsch–Butland-interpolation proposed a modified technique to simplify the Fritsch–Carlson algorithm [**16**]. In this method, the first derivatives at the nodes are calculated using Brodlie's formula. The Fritsch–Butland algorithm is local, C^1 continuous and very efficient. A rather complete analysis is given in references [**17**] and [**18**].

$f(x)$ is a function on the partition $x_0 < x_1 < \cdots < x_{n-1}$ for which $f(\boldsymbol{x}_k) = \boldsymbol{y}_k$. It is a piecewise polynomial function that consists of $n-1$ cubic polynomials f_k defined on the range $[\boldsymbol{x}_k, \boldsymbol{x}_{k+1}]$. Furthermore, each f_k is joined at $\boldsymbol{x}_k$, for $k = 1, \ldots, n-2$, such that $\boldsymbol{y}'_k = f'(\boldsymbol{x}_k)$ and $\boldsymbol{y}''_k = f''(\boldsymbol{x}_k)$ are continuous.

The kth polynomial curve, f_k, is defined over the fixed interval $[\boldsymbol{x}_k, \boldsymbol{x}_{k+1}]$ and has the cubic form

$$f_k(x) = a_k \cdot (x - \boldsymbol{x}_k)^3 + b_k \cdot (x - \boldsymbol{x}_k)^2 + c_k \cdot (x - \boldsymbol{x}_k) + d_k \tag{23}$$

where

$$a_k = \frac{1}{\Delta \boldsymbol{x}_k^2} \cdot \left(-2 \cdot \frac{\Delta \boldsymbol{y}_k}{\Delta \boldsymbol{x}_k} + \boldsymbol{y}'_k + \boldsymbol{y}'_{k+1} \right) \tag{24}$$

$$b_k = \frac{1}{\Delta \boldsymbol{x}_k} \cdot \left(3 \cdot \frac{\Delta \boldsymbol{y}_k}{\Delta \boldsymbol{x}_k} - 2 \cdot \boldsymbol{y}'_k - \boldsymbol{y}'_{k+1} \right) \tag{25}$$

$$c_k = \boldsymbol{y}'_k \tag{26}$$

$$d_k = \boldsymbol{y}_k \tag{27}$$

In the expression for a_k and b_k, Δx and Δy are given by

$$\begin{aligned} \Delta \boldsymbol{x}_k &= \boldsymbol{x}_{k+1} - \boldsymbol{x}_k \\ \Delta \boldsymbol{y}_k &= \boldsymbol{y}_{k+1} - \boldsymbol{y}_k \end{aligned} \tag{28}$$

for $k = 0, \ldots, n-2$.

The expressions for the cubic polynomial coefficients are given in terms of position data and derivatives. The first derivatives at the nodes are calculated by using Brodlie's formula with

$$f'(\boldsymbol{x}_k) = \frac{m_{k-1} \cdot m_k}{\alpha \cdot m_k + (1 - \alpha) \cdot m_{k-1}} \tag{29}$$

$$m_k = \frac{\Delta \boldsymbol{y}_k}{\Delta \boldsymbol{x}_k} \tag{30}$$

$$\alpha = \frac{\Delta \boldsymbol{x}_{k-1} + 2 \cdot \Delta \boldsymbol{x}_k}{3 \cdot (\Delta \boldsymbol{x}_{k-1} + \Delta \boldsymbol{x}_k)} \tag{31}$$

The Fritsch–Butland interpolation is a special type of a cubic spline interpolation. The algorithm is rather efficient and leads nevertheless to sufficiently accurate results.

4.3.2 *Generalized cubic spline interpolation*

The generalized cubic spline interpolation, especially the usage of a rational spline is discussed in this section. The goal of rational spline interpolation is to get an interpolation formula that is smooth in the first derivative and continuous in the second derivative, both within an interval and at its boundaries. A detailed analysis is given in references [**19**] and [**20**].

Given is a tabulated function of nodes $(\boldsymbol{x}_k, \boldsymbol{y}_k)$ with $x_1 < \cdots < x_n$ for $k = 1, \ldots, n$, where $\boldsymbol{x}_k$ represents the data site and $\boldsymbol{y}_k$ the data values at site $\boldsymbol{x}_k \cdot \boldsymbol{f}_k$ is a smooth, piecewise C^2 continuous function and is restricted on the subinterval $[\boldsymbol{x}_k, \boldsymbol{x}_{k+1}]$

$$f_k(x) = A_k \cdot u + B_k \cdot t + C_k \cdot \frac{u^3}{p \cdot t + 1} + D_k \cdot \frac{t^3}{p \cdot u + 1} \tag{32}$$

The variables t, u, Δx, A_k, B_k, and C_k are given by

$$t = \frac{x - \boldsymbol{x}_k}{\Delta \boldsymbol{x}_k} \tag{33}$$

$$u = 1 - t \tag{34}$$

$$\Delta \boldsymbol{x}_k = \boldsymbol{x}_{k+1} - \boldsymbol{x}_k \tag{35}$$

$$A_k = \boldsymbol{y}_k - C_k \tag{36}$$

$$B_k = \boldsymbol{y}_k - D_k \tag{37}$$

$$C_k = \frac{\begin{array}{c}(3+p) \cdot \Delta \boldsymbol{y}_k - (2+p) \cdot \Delta \boldsymbol{x}_k \cdot \Delta \boldsymbol{y}'_k \\ -\Delta \boldsymbol{x}_k \cdot \boldsymbol{y}'_{k+1}\end{array}}{(2+p)^2 - 1} \tag{38}$$

$$D_k = \frac{\begin{array}{c}-(3+p) \cdot \Delta \boldsymbol{y}_k + \Delta \boldsymbol{x}_k \cdot \Delta \boldsymbol{y}'_k \\ +(2+p_k) \cdot \Delta \boldsymbol{x}_k \cdot \Delta \boldsymbol{y}'_{k+1}\end{array}}{(2+p)^2 - 1} \tag{39}$$

The expressions of the coefficients A_k, B_k, C_k, and D_k are given in terms of the parameter p as well as the position data and its derivatives. The parameter p controls the smoothness of the interpolated function f_k and is defined in the range $p \in (-1, \infty)$.

The smoothness of the interpolated function can be handled directly by adjusting the parameter p – increasing p leads to increased smoothness. Because of the fact that only positions are given, the derivative values have to be determined by solving the following system

$$\frac{1}{\Delta \boldsymbol{x}_{k-1}} \cdot \boldsymbol{y}'_{k-1} + (2+p) \cdot \left(\frac{1}{\Delta \boldsymbol{x}_{k-1}} + \frac{1}{\Delta \boldsymbol{x}_k} \right) \cdot \boldsymbol{y}'_k + \frac{1}{\Delta \boldsymbol{x}_k} \cdot \boldsymbol{y}'_{k+1} = (3+p) \cdot \left[\frac{\Delta \boldsymbol{y}_{k+1}}{\Delta \boldsymbol{x}_{k-1}^2} + \frac{\Delta \boldsymbol{y}_k}{\Delta \boldsymbol{x}_k^2} \right] \tag{40}$$

Thus, a tri-diagonal system of equations (interpolation in circumferential direction) as well as a cyclical tri-diagonal system of equations (interpolation in radial or axial direction) that relate the unknown derivatives to the position data needs to be solved by using an LU decomposition [**19**].

Interpolation with rational cubic spline functions leads to smooth and accurate interpolation results.

4.4 Integration of the pressure distribution

In order to apply the forces to the coupled FE-nodes, the hydrodynamic pressure distributions have to be integrated. Therefore a two-dimensional space integration, which is based on the isoparametric coordinate transformation, is used. Analogous to the numerical interpolation and the solution of the contact equation, the integration is done in the cylindrical joint coordinate system. For the investigations detailed results are shown applying linear and tetragonal FEM meshes of the contacting surfaces.

The integration is done in two steps. First, the pressure distribution on the calculation grid (Fig. 1) has to be integrated by multiplication of the discrete pressure values with the corresponding surface areas. Afterwards the calculated forces need to be transformed from the calculation grid to the coupled FEM grids of the two bodies. Therefore an isoparametric transformation is used, as it is defined in reference [**21**] for linear and tetragonal FEM topologies.

$$\begin{aligned} x(\xi,\eta) &= \sum_{k=1}^{4} \boldsymbol{x}_k \cdot N_k(\xi,\eta) \\ y(\xi,\eta) &= \sum_{k=1}^{4} \boldsymbol{y}_k \cdot N_k(\xi,\eta) \end{aligned} \tag{41}$$

where the corresponding linear shape functions are given by

$$\begin{aligned} N_1(\xi,\eta) &= \frac{1}{4} \cdot (1+\xi) \cdot (1+\eta) \\ N_2(\xi,\eta) &= \frac{1}{4} \cdot (1-\xi) \cdot (1+\eta) \\ N_3(\xi,\eta) &= \frac{1}{4} \cdot (1-\xi) \cdot (1-\eta) \\ N_4(\xi,\eta) &= \frac{1}{4} \cdot (1+\xi) \cdot (1-\eta) \end{aligned} \tag{42}$$

In equation (41), the vector $(\boldsymbol{x}_k, \boldsymbol{y}_k)$ contains the coordinates of the FE-node with index k. After integration of the pressure to forces, the forces have to be divided on the four FE-nodes of the corresponding FE-element by using the shape functions N_1, N_2, N_3, and N_4 from the isoparametric transformation (42).

5 SIMULATION MODEL

For the investigations of the surface contact algorithm, referring to sections 2, 3, and 4, two axial thrust bearings of a four cylinder combustion engine with a constant engine running condition of 1800 r/min is utilized. The crankshaft and the power unit are modelled on the basis of three-dimensional solid FEM models (Fig. 4) and the connecting rods (conrods), the pistons as well as the piston-pins are given by beam mass models. The five main bearings as well as the small end and big end bearings

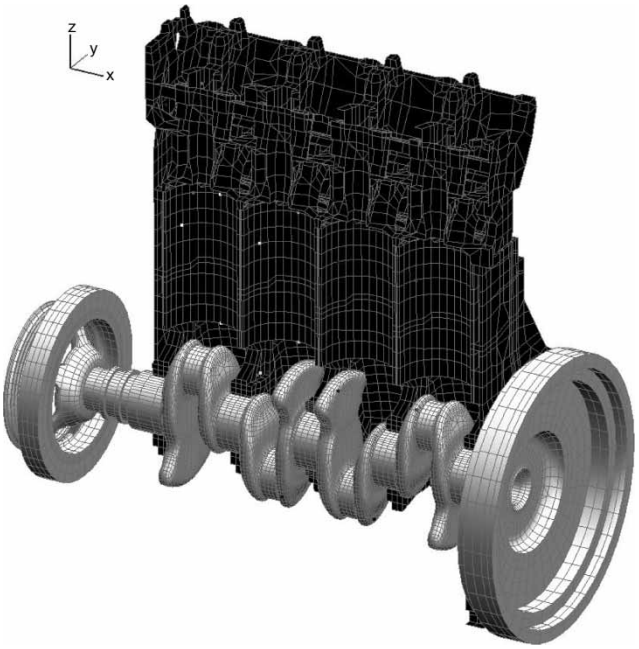

Fig. 4 FEM-bodies of the power unit (cross-section) and the crankshaft

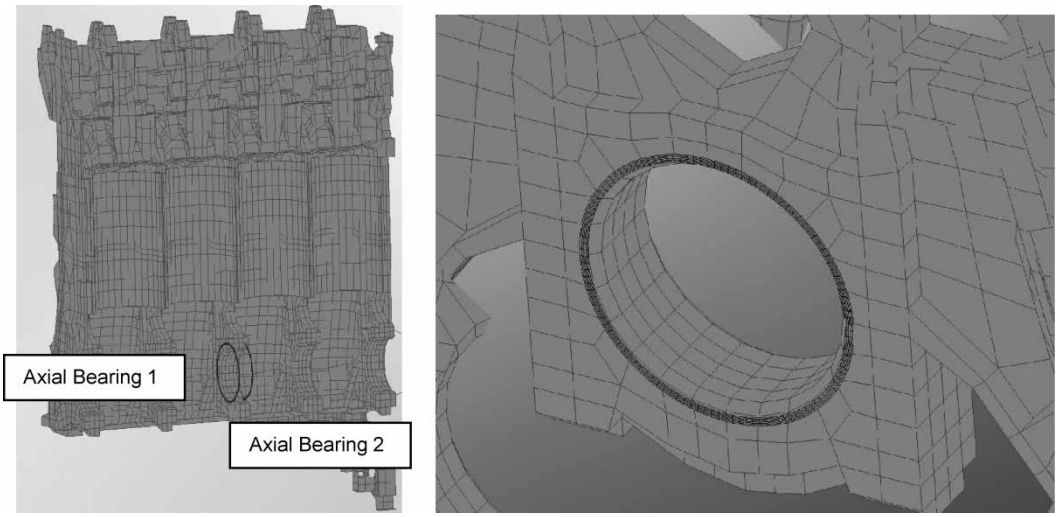

Fig. 5 FE-grid of the power unit and the hydrodynamic calculation grids: cross-sectional view of the power unit and of the two investigated axial bearings (left), detailed view of axial bearing 2 (right)

of the four conrods are represented by non-linear spring-damper functions.

The focus of the investigation is put on the surface contacts of the axial thrust bearings between the crankshaft and the engine block. Figure 5 shows the surface contact areas of the two axial thrust bearings. Although the body surfaces are given by rough FEM meshes, the lubricated contact is determined on the fine calculation grid.

Therefore, only linear and tetragonal FEM topologies of the contacting bodies are used. Each axial slider bearing is coupled with two radial node sections at the power unit and with three radial node sections at the crankshaft. Furthermore, each radial section contains 48 nodes in circumferential direction. The corresponding calculation domain for the surface contact evaluation is defined with 11 radial sections and 120 circumferential nodes persection.

Figure 6 depicts the cylinder pressure curves that are obtained by measurement data. The combustion

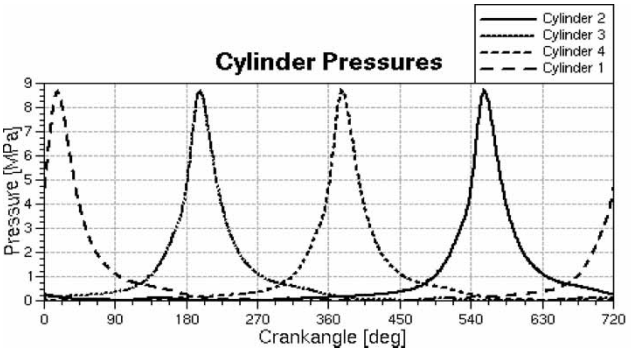

Fig. 6 Pressure curves of the four cylinder

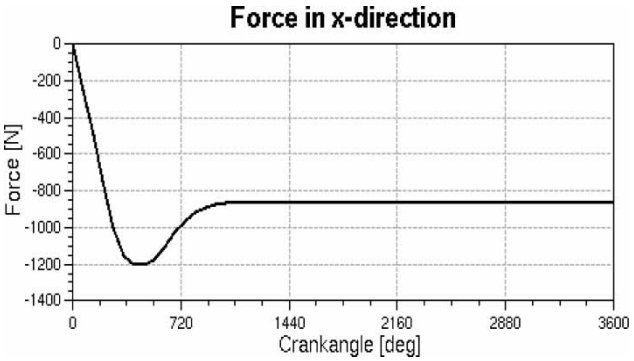

Fig. 7 Axial force characteristic due to disengage of the clutch

pressures (maximum: 8.6 MPa) have to be applied to the small end bearings of the corresponding conrods.

In addition to the cylinder pressures, a mean output torque of 231 000 N mm has to be applied to the crankshaft, in order to ensure the balance of forces and moments.

Furthermore, an axial force characteristic (Fig. 7), which represents the axial force function concerning disengaging of a clutch, is applied to the crankshaft.

For the investigations, a flexible multi-body dynamics-simulation-program [**22**] is used. Therefore, five cycles, equivalent to 0.3 s are calculated using an adaptive control of the time step size.

6 RESULTS AND DISCUSSION

The calculated results are presented and discussed in this section. Figure 8 shows the five engine cycles of

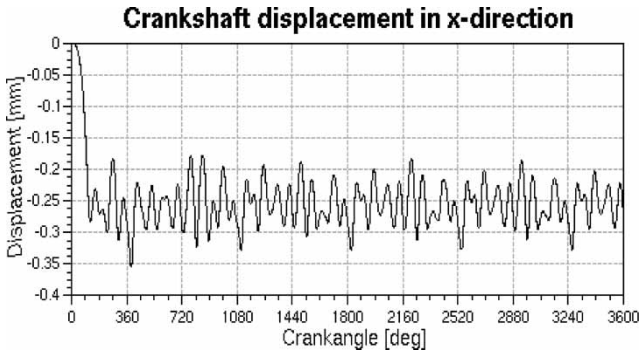

Fig. 8 Crankshaft displacement in axial direction of the five engine cycle

the global axial crankshaft displacement (x-direction) for the simulation model introduced in section 5.

In order to guarantee that the simulation model is steady state, the differences of the axial displacement of the crankshaft between the fourth and the fifth engine cycle is depicted in Fig. 9. Because of the maximum amplitude of just 0.0064, the simulation model is initialized to 96.4 per cent in the fifth cycle. Thus, the next results will only be displayed for the fifth cycle.

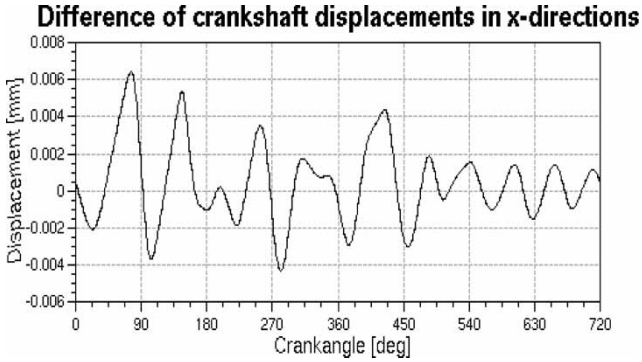

Fig. 9 Difference of the crankshaft displacements between the fourth and the fifth cycle in axial direction

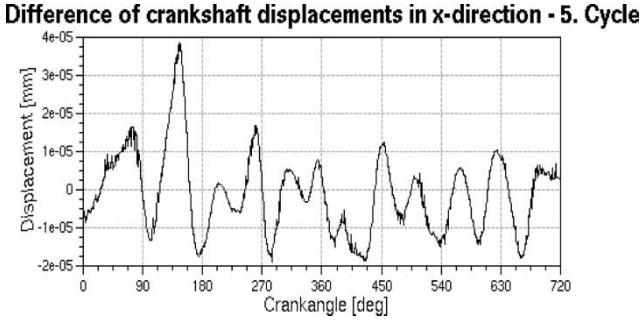

Fig. 10 Differences of crankshaft displacements according to the Fritsch–Butland interpolation and the generalized cubic spline interpolation

For the investigations of the surface contact evaluation different numerical interpolation approaches (referring to section 4.3) for the determination of the clearance gap and its first derivative in time are utilized. Figure 10 shows the differences of the crankshaft displacements in axial direction of the fifth engine cycle according to the used interpolation methods. It can be seen that the differences of the crankshaft displacements between the Fritsch–Butland-interpolation and the generalized cubic spline approach are negligible small, but a comparison of CPU times for the different interpolation approaches reflects a significant difference. By the usage of the more costly approach (generalized cubic spline) the convergence of the entire simulation process is getting better and consequently the CPU time decreases. It can be recognized that for the generalized cubic spline interpolation, the simulation process requires 8 per cent less CPU time than for the Fritsch–Butland approach (Table 1).

The same tendency can be observed for running conditions of 1600 and 2000 r/min as in the previous table depicted. This behaviour is caused by the high sensitivity of the elastohydrodynamic contact evaluation in terms of the clearance gap and the first time derivative. A more accurate and smooth interpolated gap between the contacting surfaces leads to a better convergence of the surface contact evaluation.

The resultant forces that are obtained by the axial contact evaluations are depicted in Fig. 11 for the fifth engine cycle. The resultant contact force in the axial thrust bearing 1 can be seen to be negligible because of the defined axial force characteristic (Fig. 7).

Table 1 Comparison of the CPU times taken by using different interpolation approaches

CPU time for Fritsch–Butland (s)	CPU time for generalized cubic spline (s)	Running condition (r/min)
96 093.75	91 268.10	1600
70 717.28	65 446.29	1800
89 934.45	84 245.53	2000

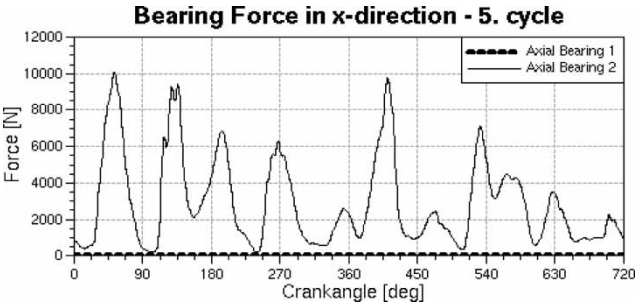

Fig. 11 Resultant forces of the axial thrust bearings that act on the crankshaft

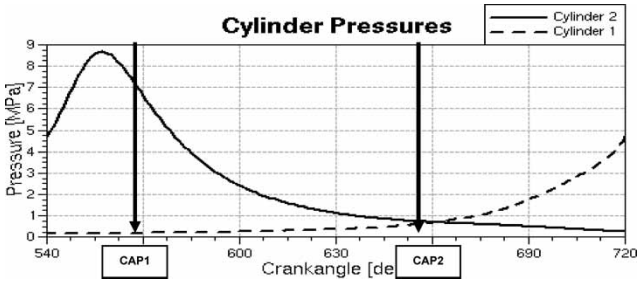

Fig. 12 Crankshaft angular position 1 (CAP1) and crankshaft angular position 2 (CAP2)

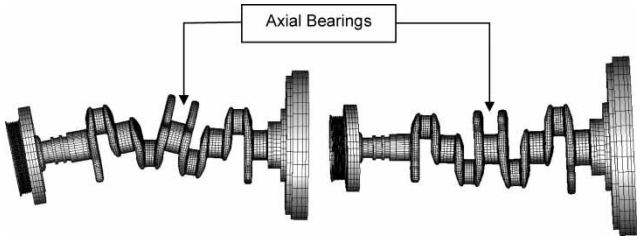

Fig. 13 Large-scaled crankshaft deformations at CAP1 and CAP2

For the results of the axial thrust bearings, two crankshaft angular positions of the fifth engine cycle are selected, as shown in Fig. 12. The first crankshaft position (CAP1) is selected at 557° crank angle (CRA) (maximum combustion pressure of 8.6 MPa) and the second at 660° CRA (0.7 MPa).

Figure 13 depicts large-scaled crankshaft deformations at the corresponding crankshaft angular positions CAP1 and CAP2. By comparing the two deformed crankshafts, a significant difference of deformation shapes at the contact surfaces in the axial thrust bearings can be observed.

Table 2 Comparison of the CPU times taken by using different interpolation approaches for a simulation without combustion loads and output torque

CPU time for Fritsch–Butland (s)	CPU time for generalized cubic spline (s)	Running condition (r/min)
60 594.34	60 837.23	1600
57 678.28	57 704.29	1800

The corresponding hydrodynamic pressure distribution at the two different crankshaft deformations CAP1 and CAP2 are displayed in Fig. 14. The figure shows the hydrodynamic pressure shapes at the flange of the power unit for the axial thrust bearing 2. The left part of the figure depicts the pressure shape at CAP1 and the right part displays the shape at CAP2.

At the flange surface a contour profile with six symmetrical grooves is defined. They are equally distributed over the circumference. Thereby, each groove is designed with 25° width angle and the pressure distributions in the grooves are set zero as shown clearly in Fig. 14. By comparing the hydrodynamic pressure distributions for the two crankshaft positions (CAP1, CAP2), the different local maxima can be observed with reference to the corresponding crankshaft deformations (Fig. 13).

Further investigations have shown that the CPU times (Table 2) taken by using different interpolation approaches are almost equal. For these calculations, the simulation model, which is described in section 5

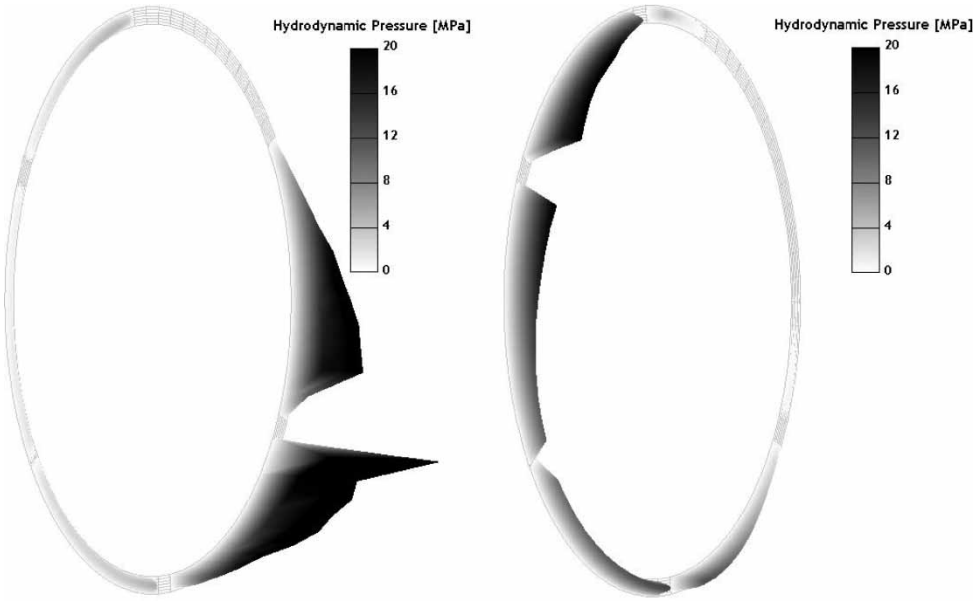

Fig. 14 Pressure distribution enlarged in axial direction of the flange of the axial bearing 2 at CAP1 and CAP2

is utilized, but without using the combustion loads and the output torque. Because of this configuration, the crankshaft deformation is almost equal allover simulation time and looks similar to the left picture of Fig. 13.

The investigation results represent, that the usage of an accurate interpolation approach instead of an efficient method leads to a better convergence of the contact evaluation and consequently the CPU time for the simulation process decreases, but this behaviour can only be observed for simulations with significant deformations of the surface contact areas.

7 CONCLUSION

A surface contact algorithm with different numerical interpolation approaches for the clearance gap and its time derivative was utilized to investigate the elastohydrodynamic behaviour of axial thrust bearings. Thereby, the modelling of the moving and flexible bodies as well as the discretization of the contact equation was represented. An efficient interpolation method (Fritsch–Butland) as well as an accurate interpolation approach (generalized cubic spline) was investigated. Detailed results for linear and tetragonal FEM meshes for the contact surfaces were shown, such as the hydrodynamic pressure distributions in terms of different deformed crankshafts in axial thrust bearings. The results outlined, that an accurate and smooth interpolation approach leads to a better simulation performance (CPU-time) for applications with large deformations of the contact surfaces.

ACKNOWLEDGEMENTS

The work described within this paper has been done by the Industrial Mathematics Competence Center (IMCC) in Linz, Austria, by the Christian Doppler Laboratory for Engine and Vehicle Acoustics in Graz, Austria, by AVL List GmbH, Graz, Austria and by the Acoustic Competence Centre in Graz, Austria.

The authors are grateful to the Bundesministerium für Wirtschaft und Arbeit, to the Government of Upper Austria within the framework of industrial competence centres and to the Christian Doppler Foundation of the Austrian Government for funding this work.

REFERENCES

1 **Gran, S.** *Mehrkörperdynamik elastischer Körper–Kurbeltrieb*. PhD Thesis, Technical University Graz, 1994.

2 **Bestle, D.** *Analyse und Optimierung von Mehrkörpersystemen*, 1994 (Springer, Berlin).

3 **Shabana, A. A.** *Vibration of discrete and continuous systems*, 2nd edition, 1997 (Springer, New York).

4 **Offner, G., Eizenberger, T.,** and **Priebsch, H. H.** Separation of reference motions and elastic deformations in an elastic multi-body system. *Proc. IMechE, Part K: J. Multi-body Dynamics*, 2006, **220**, 63–75.

5 **Offner, G.** *Multi-body dynamics and numerical methods, application for internal combustion engines*. Professorial Thesis, Technical University Graz, 2005.

6 **Silar, P.** *Numerische Untersuchung unterschiedlicher Verfahren zur Reduktion von Freiheitsgraden im Rahmen von Mehrkörperdynamik-und Körperschallberechnungen von Verbrennungsmotoren*. Diploma Thesis, Technical University Graz, 2003.

7 **Patir, N.** and **Cheng, H. S.** An average flow model for determining effects of three dimensional roughness on partial hydrodynamic lubrication. *Trans. ASME, F, J. Lubr. Technol.*, 1978, **100**, 12–17.

8 **Patir, N.** and **Cheng, H. S.** Application of average flow model to lubrication between rough sliding surfaces. *Trans. ASME, F, J. Lubr. Technol.* 1979, **101**, 220–230.

9 **Offner, G.** *Mathematische Modellierung des Kolben–Zylinder–Kontakts in Verbrennungskraftmaschinen und numerische Simulation des durch mechanischen Kolbenschlag angeregten Körperschalls.* PhD Thesis, Technical University Graz, 2000.

10 **Schwarz, H. R.** *Numerische mathematik*, 1997 (Teubner, Stuttgart).

11 **Newmark, N. M.** A method of computation for structural dynamics. *J. Eng. Mech. Div.*, 1959, **85**(3), 67–94.

12 **Roth, P. M.** *Numerische Zeitintegration zur Mehrkörperdynamik- und Körperschallberechnung*. Diploma Thesis, Technical University Graz, 2002.

13 **Eizenberger, T.** *Dynamic simulation of flexible structures undergoing large gross motion*. PhD Thesis, Johannes Keppler University Linz, 2003.

14 **Renka, R. J.** Cubic Shepard method for bivariate interpolation of scattered data. *ACM Trans. Math. Softw.*, 1999.

15 **Renka, R. J.** Multivariate interpolation of large sets of scattered data. *ACM Trans. Math. Softw.*, 1988, **14**, 139–148.

16 **Fritsch, F. N.** and **Butland, J.** A method for constructing local monotone piecewise cubic interpolants. *SIAM J. Sci. Stat. Comput.*, 1984, **5**, 300–304.

17 **Huynh, T.** Accurate monotone cubic interpolation. *SIAM J. Numer. Anal.*, 1993, **30**(1), 57–100.

18 **Wolberg, G.** and **Alfy, I.** An energy-minimization framework for monotonic cubic spline interpolation. *J. Comput. Appl. Math.*, 2002, **143**, 145–188.

19 **Späth, H.** *Eindimensionale spline-interpolations algorithmen*, 1990 (Jörg Meier Oldenbourg, Munich).

20 **Farin, G., Hoschek, J.,** and **Kim, M. S.** Handbook of computer aided geometric design, 2002, (North-Holland, Amsterdam).

21 **Bathe, K. J.** *Finite element procedures in engineering analysis*, 1982 (Prentice Hall).

22 AVL-EXCITE Reference Manuel (Version 7.0), AVL LIST GmbH, Graz, 2006.

APPENDIX

Notation

$\mathbf{A}_x$ skew symmetric matrix for any vector $\boldsymbol{x} \in R^3$ defined as

$$\mathbf{A}_x = \begin{pmatrix} 0 & -x_3 & x_2 \\ x_3 & 0 & -x_1 \\ -x_2 & x_1 & 0 \end{pmatrix}$$

c clearance
c_i position vector (geometry) of node i in the non-deformed body
d displacement
$\mathbf{D}$ damping matrix of a body
$\bar{\mathbf{D}}$ reduced damping matrix of a body
e eccentricity
$\boldsymbol{f}$ vector of forces and moments
$\boldsymbol{f}^{\text{ext}}$ vector of external forces and moments
$\boldsymbol{f}^{\text{gyros}}$ vector of gyroscopic forces and moments
$\boldsymbol{f}^{\text{rbAcc}}$ vector of rigid body accelerations
$\bar{\boldsymbol{f}}$ reduced vector of forces and moments
$\mathbf{G}_{\text{fa}}$ dynamic transformation matrix
$\bar{h}$ average film thickness in physical domain
$\overline{h_{\text{T}}}$ local film thickness
I_i mass moment of inertia of node i
$\mathbf{K}$ stiffness matrix of a body
$\bar{\mathbf{K}}$ reduced stiffness matrix of a body
m_i mass of the discrete body node i
$\mathbf{M}$ mass matrix of a body
$\bar{\mathbf{M}}$ reduced mass matrix of a body
p parameter for smoothness of the rational spline function
$\boldsymbol{q}$ vector of displacements
$\dot{\boldsymbol{q}}$ vector of velocities
$\ddot{\boldsymbol{q}}$ vector of accelerations
$\boldsymbol{q}_a$ reduced vector of displacements
$\boldsymbol{q}_t$ vector of physical degrees of freedom
r radial coordinate
R_{in} flange/thrust external radius
R_{out} flange/thrust internal radius
t time
w speed in radial direction
$\boldsymbol{u}_i$ local displacement vector of node i
u speed in ϕ-direction
$\boldsymbol{x}_{\text{B}}$ global position vector of a body
y coordinate in film thickness direction
$\boldsymbol{z}$ vector of modal degrees of freedom
δ_1, δ_2 random roughness amplitudes with Gaussian distribution
η dynamic viscosity
$\bar{\theta}$ fill ratio ($0 < \bar{\theta} < 1$)
κ tilt angle
σ_{c} composite RMS roughness
σ_1, σ_2 standard deviation of clearance gap at thrust and flange surfaces
ϕ circumferential coordinate
Φ_x pressure flow factor in circumferential direction
$\Phi_{\bar{z}}$ pressure flow factor in radial direction
Φ_{s} shear flow factor
$\boldsymbol{\omega}_i$ vector of local angular velocities of node i
Ω angular velocity vector of a body